# Guiding Spatial Arrangements of Silver Nanoparticles by Optical Binding Interactions in Shaped Light Fields

**Zijie Yan,[†] Raman A. Shah,[†] Garrett Chado,[†] Stephen K. Gray,[‡] Matthew Pelton,[‡] and Norbert F. Scherer[†,‡,*]**

[†]Department of Chemistry and The James Franck Institute, The University of Chicago, 929 East 57th Street, Chicago, Illinois 60637, United States and
[‡]Center for Nanoscale Materials, Argonne National Laboratory, 9700 South Cass Avenue, Argonne, Illinois 60439, United States

**ABSTRACT** We demonstrate assembly of spheroidal Ag nanoparticle clusters, chains and arrays induced by optical binding. Particles with diameters of 40 nm formed ordered clusters and chains in aqueous solution when illuminated by shaped optical fields with a wavelength of 800 nm; specifically, close-packed clusters were formed in cylindrically symmetric optical traps, and linear chains were formed in line traps. We developed a coupled-dipole model to calculate the optical forces between an arbitrary number of particles and successfully predicted the experimentally observed particle separations and arrangements as well as their dependence on the polarization of the incident light. This demonstrates that the interaction between these small Ag particles and light is well described by approximating the particles as point dipoles, showing that these experiments extend optical binding into the Rayleigh regime. For larger Ag nanoparticles, with diameters of approximately 100 nm, the optical-binding forces become comparable to the largest gradient forces in the optical trap, and the particles can arrange themselves into regular arrays or synthetic photonic lattices. Finally, we discuss the differences between our experimental observations and the point dipole theory and suggest factors that prevent the Ag nanoparticles from aggregating as expected from the theory.

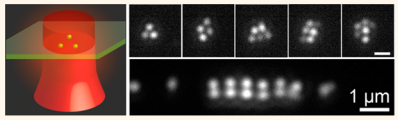


**KEYWORDS:** optical binding · Ag nanoparticles · Rayleigh regime · self-assembly · light–matter interaction · optical tweezers

The assembly of nanomaterials for specific functions is of both fundamental and applied interest. Self-assembly methods have been widely studied, including both the assembly of equilibrium structures, driven by the minimization of free energy, and the dynamic assembly of nonequilibrium structures, driven by the interaction between gradients or external fields and dissipative processes.[1−4] A greater degree of control can be obtained by directed assembly, through chemical functionalization of the nanoparticles, through the use of physical or chemical templates, or through the application of static or time-varying electrical or magnetic fields.[3−8] The range of materials and structures that could be formed would be expanded if other driving forces and nanomaterial interactions could be harnessed. In this paper we use an applied (optical) field that induces an interparticle potential, resulting in defined spatial configurations of metal nanoparticles.

Optical binding can be viewed as a form of directed assembly, induced through the application of optical-frequency electromagnetic fields.[9,10] When light is incident on polarizable particles, the incident field and light scattered from the particles interfere, leading to spatial gradients in the field; these gradients, in turn, induce forces on the particles, and the particles rearrange until these forces disappear. The interparticle forces arise even if the incident field has no potential gradient; in this sense, the particles self-direct their own assembly. The optically induced interactions occur over a range of length scales. For example, near-field interactions occur for interparticle separation distances $d \ll \lambda$ (which could be used to create hot nanoparticle pairs[11] and aggregates,[12] and the local field enhancements have been used to increase the sensitivity of Raman spectroscopy[13]), and far-field interactions occur for $d \gg \lambda$. The optical binding interaction is intermediate between these two limits: optically bound particles are typically separated by distances that are integral multiples of the wavelength of the incident light in the host medium.[9,14]

Due to the simplicity of the requisite experimental conditions, there have been

* Address correspondence to nfschere@uchicago.edu.

Received for review December 21, 2012 and accepted January 30, 2013.

**Published online January 30, 2013**
**10.1021/nn3059407**

many reports of optical binding.[15,16] However, nearly all of the experimental realizations of optical binding have been of particles whose sizes are comparable to or larger than the wavelength, $\lambda$, of light.[16,17] By contrast, the simplest theoretical description of optical binding treats the particles as point dipoles.[9,16,18,19] In order for this model to provide an accurate description, the radius, $a$, of the particles undergoing optical binding would need to be small enough that the particles can be well approximated as point dipoles; that is, the particles need to be in the Rayleigh regime such that $ka \ll 1$, where $k$ is the wavenumber of light in the medium. This has not yet been demonstrated, but a very recent report that appeared while our article was in preparation comes close.[20] Their report showed "ultrastrong" optical binding of pairs of Au particles with diameters of 200 nm, corresponding to $ka = 0.8$. The authors suggested that optical binding of particles with diameters of 45 nm or even less should also be possible.[20]

Furthermore, optical binding of more than two nanoparticles has yet to be studied systematically. For such a system, the dipole model (for two nanoparticles)[16] itself must be generalized to an arbitrary number of particles.

In this article, we demonstrate the optical binding of Ag nanoparticles with diameters of 40 nm. These are the smallest particles yet shown to exhibit optical-binding interactions and bring experimental studies of optical binding into the Rayleigh regime. The binding occurs between particles that are held in optical Bessel beams or optical line traps. These shaped optical fields induce external potentials that affect the spatial arrangements of the optically bound nanoparticles. The experimental findings are supported by a coupled-dipole model of the optical forces.[21] Our experimental arrangement allows us to study systematically the optical binding of more than two nanoparticles, and we have extended the dipole model to treat these multiparticle interactions.[20,22] We have also observed the optical binding of larger Ag nanoparticles, with diameters of approximately 100 nm, where the interparticle interactions become comparable to the gradient forces of the optical traps that hold the particles in place. In this case, regular, rigid lattice structures form. The interplay between the polarization direction and the anisotropy of the trapping field makes it possible to control the parameters of these synthetic photonic lattices.

## THEORETICAL BACKGROUND

**Coupled-Dipole Model.** In order to understand the multiparticle arrangements that we observe, we first examine the optically induced interactions that are responsible for the arrangements. In order to do so, we extend the theoretical model for optical binding in the Rayleigh regime proposed by Dholakia and Zemánek[16] from two particles to $N$ particles. In this model, the electric field, $\mathbf{E}(\mathbf{r}_n,t)$, at the position of particle $n$ is a combination of the incident oscillating electric field $\mathbf{E}^I(\mathbf{r},t) = \mathbf{E}^I(\mathbf{r})e^{-i\omega t}$ with the electric fields generated by all the other particles. This field induces a dipole moment $\mathbf{p}^{(n)}(t) = \mathbf{p}^{(n)}e^{-i\omega t}$ in particle $n$ according to its polarizability tensor: $p_s^{(n)} = \alpha_{st}^{(n)}E_t(\mathbf{r}_n)$. In this equation, and in the following, $m$ and $n$ index the particles in the system and range from 1 to $N$; the symbols $s$, $t$, $u$, $v$, and $w$ index the spatial directions $x$, $y$, and $z$, and summation over these indices is assumed when they are repeated in a term. For example, the equation $p_s^{(n)} = \alpha_{st}^{(n)}E_t(\mathbf{r}_n)$ is shorthand for the $3N$ equations:

$$p_x^{(1)} = \sum_{t\in\{x,y,z\}} \alpha_{xt}^{(1)}E_t(\mathbf{r}_1), \ldots,$$
$$p_z^{(N)} = \sum_{t\in\{x,y,z\}} \alpha_{zt}^{(N)}E_t(\mathbf{r}_N) \quad (1)$$

The dyadic Green function defines how the oscillating dipole, $\mathbf{p}^{(m)}$, of a distinct particle $m$ contributes to the electric field, $\mathbf{E}(\mathbf{r}_n)$, at the position of particle $n$:[16]

$$G_{st}(\mathbf{r}_n,\mathbf{r}_m) = \frac{\exp(ikR)}{4\pi\varepsilon_0\varepsilon_m R^3}\left[(3 - 3ikR - k^2R^2)\frac{R_sR_t}{R^2} + (k^2R^2 + ikR - 1)\delta_{st}\right] \quad (2)$$

In this equation, $R$ is the magnitude of the displacement $\mathbf{R} = \mathbf{r}_n - \mathbf{r}_m$; $k = 2\pi/\lambda$ is the wavenumber of light in the medium; $\varepsilon_0$ and $\varepsilon_m$ are the permittivity of free space and the relative permittivity of the medium, respectively; and $\delta_{st}$ is the Kronecker delta. The fields at each of the dipoles can thus be written as a coupled system of $3N$ linear equations that can be solved numerically:

$$E_s(\mathbf{r}_n) = E_s^I(\mathbf{r}_n) + \sum_{m\neq n} G_{st}(\mathbf{r}_n,\mathbf{r}_m)\alpha_{tu}^{(m)}E_u(\mathbf{r}_m) \quad (3)$$

Once this system of equations has been solved, the optical force on each particle can be calculated from the field at the location of the particle and its gradient:[16,23]

$$F_s^{(n)} = \frac{1}{2}\mathrm{Re}\left[p_t^{*(n)}\frac{\partial E_t(\mathbf{r})}{\partial r_s}\bigg|_{\mathbf{r}=\mathbf{r}_n}\right] = \frac{1}{2}\mathrm{Re}\left[\alpha_{tu}^{*(n)}E_u^*(\mathbf{r}_n)\frac{\partial E_t(\mathbf{r})}{\partial r_s}\bigg|_{\mathbf{r}=\mathbf{r}_n}\right] \quad (4)$$

The derivative of the field in eq 4 can be expanded from eq 3 by analytically computing the partial derivatives of the incident field as well as of the Green function. This finally gives a formula for the optical force:

$$F_s^{(n)} = \frac{1}{2}\mathrm{Re}\left\{\alpha_{tv}^{*(n)}E_v^*(\mathbf{r}_n)\left[\frac{\partial E_t^I(\mathbf{r})}{\partial r_s}\bigg|_{\mathbf{r}=\mathbf{r}_n} + \sum_{m\neq n}\left(\frac{\partial G_{tu}(\mathbf{r},\mathbf{r}_m)}{\partial r_s}\bigg|_{\mathbf{r}=\mathbf{r}_n}\alpha_{uw}^{(m)}E_w(\mathbf{r}_m)\right)\right]\right\} \quad (5)$$

**Theoretical Predictions.** We used this model to calculate the forces among Ag nanoparticles with diameters

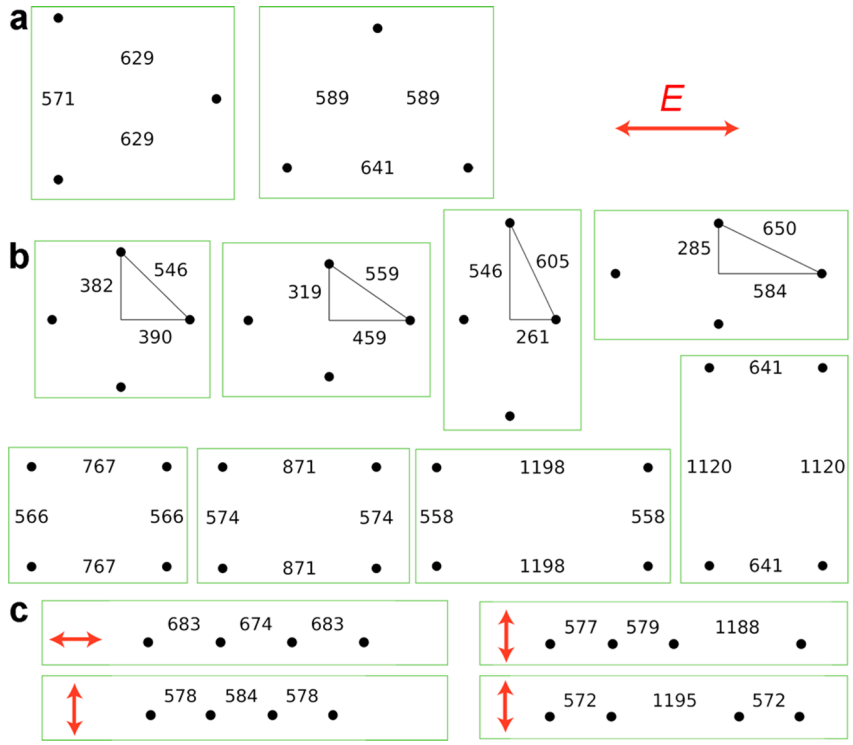


**Figure 1. Equilibrium configurations of (a) three and (b) four Ag nanoparticles with 40 nm diameters, organized by optical binding in a two-dimensional light field. The red arrow indicates the polarization direction for all these cases. (c) Equilibrium configurations for four Ag nanoparticles arranged in a quasi-one-dimensional light field. The polarization direction is indicated by the arrow for each case. Distances are shown as numbers in units of nanometers.**

of 40 nm that are confined on a two-dimensional (2D) surface and illuminated by a linearly polarized plane wave incident normal to the surface; details of the calculations are described in the Methods section. The calculations predict several trends for the spatial arrangements of Ag nanoparticles in different light fields.

For three and four Ag nanoparticles in a 2D light field, the calculations show a variety of stable equilibrium configurations, as exhibited in Figure 1a and b. With three nanoparticles, triangles are formed (Figure 1a), but the polarization of the light (weakly) breaks the symmetry of optical binding, giving rise to isosceles rather than equilateral triangles. Similarly, for four particles, the stable optically bound configurations are rectangles and rhombi rather than squares, as seen in Figure 1b. The rich set of predicted configurations suggests a complicated potential energy surface.

For multiple Ag nanoparticles in a quasi-one-dimensional (quasi-1D) light field, the optical binding forces will arrange the particles in a chain. However, the coupled-dipole model predicts that optical polarization perpendicular to the chain gives particle spacings 10−15% smaller than polarization parallel to the chain. (We label this prediction 1, for comparison to experimental results below.) The predicted interparticle separations are around 600 nm, which is nearly equal to the wavelength of the trapping laser in the water/glycerol medium (800 nm in vacuum). An example with four particles is shown in Figure 1c, and chains with other particle numbers can be seen in the Supporting Information (Figure S1). Figure 1c also shows stable configurations with spacings approximately equal to twice the distances in the regular configurations (prediction 2; see Supporting Information, Figure S2 for chains with other particle numbers). These calculations predict subtler trends as well. In particular, for parallel polarization, the interparticle separation decreases with increasing chain length, and terminal particles at the ends of the chains are farther from their neighbors than the central particles are. For perpendicular polarization, the interparticle separation increases with increasing chain length, and the terminal particles are closer to their neighbors than the central particles are (prediction 3).

## EXPERIMENTAL RESULTS

**Experimental Setup.** Optical binding of Ag nanoparticles was studied using the optical tweezers apparatus illustrated in Figure 2a. Two kinds of structured light fields, namely, a cylindrically symmetric light field (Bessel trap) and a quasi-1D light field (line trap), were created by phase modulation of a Gaussian laser beam using a 2D spatial light modulator (SLM). The phase masks on the SLM used to create these two light fields are shown in Figure 2b. The trapping potentials are designed to confine multiple Ag nanoparticles in 2D next to the upper glass surface of the sample cell, but

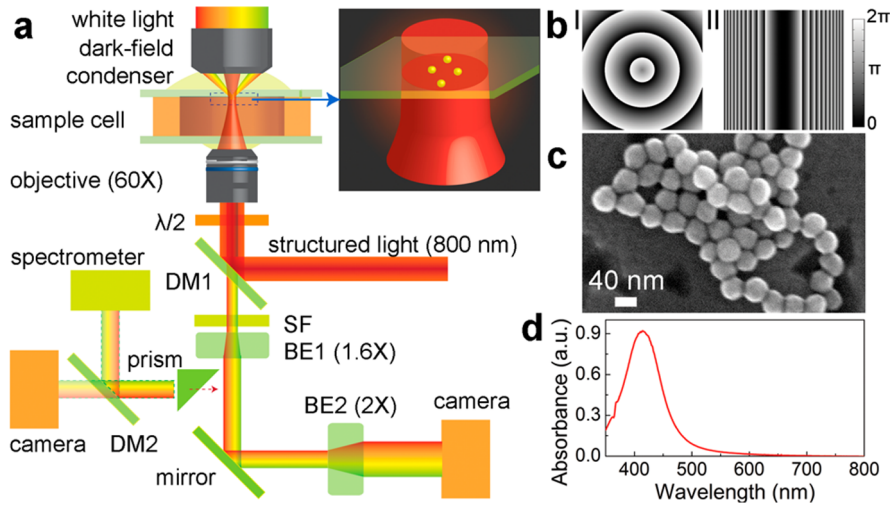


**Figure 2. (a) Experimental setup used for optical binding and dark-field microscopy of Ag nanoparticles. $\lambda/2$: half-waveplate; DM: dichroic mirror; SF: short-pass filter (cutoff at 750 nm); BE: beam expander. By inserting the prism into the scattering light path, correlated scattering spectra and optical images can be measured simultaneously. The structured light is generated by a spatial light modulator (SLM) and focused by an objective onto the surface of the top coverslip in the sample cell. The Ag nanoparticles in aqueous solution are weakly confined in the focused light field and interact with each other near the surface. (b) Phase mask profiles on the SLM used to create the (I) zero-order Bessel and (II) line-trap potentials. (c) Scanning electron microscopy (SEM) image of the Ag nanoparticles used in the experiments. (d) Absorption spectrum of the Ag nanoparticles in aqueous solution.**

to still allow the particles to undergo Brownian motion within the traps. The Ag nanoparticles are nearly monodisperse, with diameters of 40 nm (Figure 2c) and a surface plasmon resonance peak at 414 nm (Figure 2d). We also studied larger Ag nanoparticles with diameters of about 100 nm that exhibit stronger interactions. Details of the optical system and the sample preparation are provided in the Methods section.

In this paper, we define the horizontal direction of an image as the *x*-axis, the light propagation direction as the *z*-axis, and the angle between the light polarization direction and the *x*-axis as $\theta$. The orientation of an optically bound dimer or chain of nanoparticles is characterized by the angle, $\varphi$, between the interparticle axis and the *x*-axis, and the separation of two nanoparticles *i* and *j* is characterized by the distance, $d_{ij}$, between the centers of the two particles. Since a chain of particles in a line trap is usually aligned along the long axis of the trap, we also use $\varphi$ to describe the orientation of the line trap.

**Ordered Clusters of Ag Nanoparticles in a Cylindrically Symmetric Light Field.** Figure 3 demonstrates the optical binding of two Ag nanoparticles in a cylindrically symmetric light field, *i.e.*, the central spot of a zero-order Bessel beam that was linearly polarized. Figure 3a.I–III shows representative optical images of a dimer, a pair of optically bound nanoparticles, for different polarization directions. For horizontal polarization ($\theta = 0°$), the positions of the two nanoparticles as determined by centroid localization[24] are shown in Figure 3b over a trajectory of 2 s. The annular trajectories indicate that the two particles were always separated by a nonzero distance, corresponding to a repulsive interaction between the two particles. In contrast, when a single Ag nanoparticle was in the Bessel beam, it was always confined near the center of the trap (see Supporting Information, Figure S3a). Histograms of the dimer interparticle separation are shown in Figure 3c for three different polarization directions. In all cases, the equilibrium separation is approximately 600 nm. The dimers of 40 nm Ag nanoparticles exhibit polarization-dependent laser-induced orientation. It can be seen in Figure 3d that the dimer shows a weak but significant preference to align parallel to the polarization direction. (Note that we are combining the 1−2 and 2−1 dimer orientations so that, for example, an orientation of −90° is equivalent to an orientation of 90°.) The preferred separation and orientation can also be seen from the probability density distribution shown in Figure 3e, which indicates that the dimer tends to be parallel to the polarization direction (*i.e.*, 0°) and be separated by about 600 nm.

Theoretical models of optical binding indicate that optically bound dimers should prefer to be oriented perpendicular to the optical polarization.[18] This is also predicted by our coupled-dipole model and is observed for 100 nm Ag particles (see below). We believe that the anomalous behavior we observe for dimers of 40 nm Ag particles is a result of the confining field of the Bessel trap. The gradient force of the Bessel beam pushes each of the particles toward the center of the trap, as is apparent from the strong preference of a single 40 nm particle to be located near the center of the trap (see Supporting Information, Figure S3b). This radial confining force reduces the interparticle separations of the dimer particles, yet the repulsive portion of

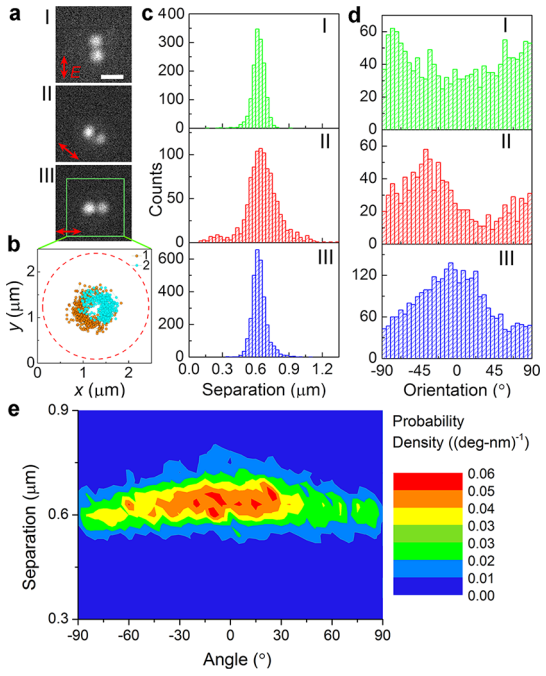


**Figure 3. Optical binding of two Ag nanoparticles in a cylindrically symmetric light field (Bessel beam) near a transparent substrate. (a) Typical images of Ag dimers formed by optical binding with different polarization directions that are indicated by the red arrows (I, $\theta = 0 \pm 4°$; II, $\theta = -45 \pm 4°$; III, $\theta = -90 \pm 4°$). The scale bar is 1 $\mu$m. (See Supporting Information, Movie S1.) (b) Typical trajectories of the two particles over a period of 2 s. The time step is 5 ms (*i.e.*, a frame rate of 200 Hz). The dashed circle represents the approximate size of the light field at the 10% intensity point. (c) Histograms of the interparticle separation and (d) histograms of the dimer orientation corresponding to the cases I−III in panel a. (e) Probability density distribution of a dimer as a function of the interparticle separation and orientation. The orientation is represented by the angle relative to the polarization direction, namely, with the value of $\varphi - \theta$ so that along the polarization is 0°. Therefore, we can combine all the data of cases I−III to calculate the probability density distribution.**

the optical-binding potential (for perpendicular orientation; see Figure 10) prevents the particles from getting too close. The spring constant for optical binding (see Figure 11) is stiffer for orientation perpendicular to the polarization direction, so it is harder to compress the dimer by the trapping potential in this direction and the confining force favors the dimer rotation to the parallel orientation, where the confining effect can be stronger. Note that the distribution contour in Figure 3e is asymmetric and that the preferred separation is about 630 nm at 0°, but it is about 580 nm at 90° (and also −90°). Theoretical calculation shows the equilibrium separation purely due to the optical binding force should be 704 nm at 0° and 562 nm at 90° for a dimer (Supporting Information, Figure S1), so the preferred separation at 0° is further away from the equilibrium separation, consistent with the idea of a stronger confining effect at 0°.

This is an example of a general phenomenon that we observe and report in this paper: nanoparticles in

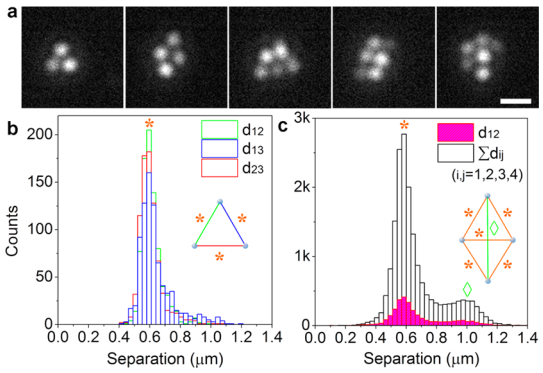


**Figure 4. (a) Optical images of three to six optically bound Ag nanoparticles in a cylindrically symmetric light field. The scale bar is 1 $\mu$m. (See Supporting Information, Movie S1.) (b) Histograms of the separation between adjacent particles in a trimer formed by optical binding. (c) Histograms of the separation between two particles in a tetramer and the sum of histograms for all possible pairs of particles, *i.e.*, distances between particles 1−2, 1−3, 1−4, 2−3, 2−4, and 3−4.**

an optical trap experience both optical-binding forces and gradient forces from the optical traps, and these forces combine to determine the configuration of particles in the trap. It is worth noting that a strongly focused laser spot with linear polarization is asymmetric, which may also induce anisotropy of the dimer orientation.[21] However, the Bessel beam has a much larger focal spot compared to a focused Gaussian beam, and by analyzing the position distribution of a single particle in the central spot of the Bessel beam, we found its intensity profile was symmetric.

When three or more 40 nm diameter Ag nanoparticles entered the central spot of the Bessel beam, they formed close-packed 2D clusters, as shown in Figure 4a. The clusters were dynamic: each single particle could move, and the entire shape could rotate and change its configuration. In addition, two particles could exchange positions with each other. That, in turn, means the sequence of particle indices are not fixed for the equilibrium geometries illustrated in Figure 4b and c. Figure S4a in the Supporting Information, for example, shows a trimer with three particles that rearranged rapidly and exhibited annular-like trajectories. The trimer did not have a preferred orientation relative to the polarization direction (see Supporting Information, Figure S4b). However, the interparticle separations remained well-defined at approximately 600 nm, corresponding to arrangement of the three particles in a nearly equilateral triangle, as shown in Figure 4b.

In a cluster of four particles, there are six particle pairs. The pink histogram in Figure 4c shows the separation of a typical pair. The other pairs have similar histograms. Since all the pairs are essentially the same in the dynamically reconfiguring cluster, we also show the histogram of interparticle separations for all the pairs. The probability distribution of interparticle separation still has a maximum at approximately 600 nm, but another broad peak centered at 1 $\mu$m is also evident.

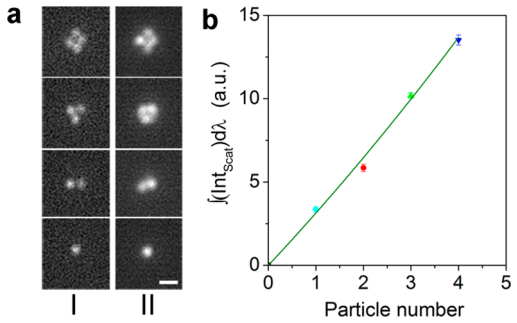


**Figure 5. (a) Dark-field optical images of one to four Ag nanoparticles in a Bessel trap and (b) the intensities of light scattered by these nanoparticles, integrated over wavelengths from 500 to 690 nm. The integration time was 0.2 s. Images in column a.I are representative optical images taken in each integration time, and images in a.II are superpositions of all images taken in that time window. (See Supporting Information, Movie S2.) The quadratic polynomial fit $f(N) = 3.04N + 0.09N^2$ shown in green indicates a slightly superlinear scaling with particle number.**

This separation corresponds to the longer diagonal of a rhombus, as illustrated in the inset of Figure 4c. Moreover, the ratio of the total counts (the black histogram in Figure 4c) for the 600 nm and the 1 $\mu$m peaks is 7.4:1 (the ratio for the pink histogram is 5.4:1), close to the ratio of 5:1 expected for an ideal rhombus.

Ordered clusters of five and six Ag nanoparticles were also observed, as illustrated in the last three images of Figure 4a. These clusters, however, were too dynamic to allow for quantitative analysis of interparticle distance.

The optical scattering from a single Ag nanoparticle and from optically bound clusters with two to four nanoparticles was studied by inserting a prism into the path of the scattered light to direct it to a spectrometer and a detector, as shown in Figure 2a. Our optical setup allows scattered light with wavelengths from 450 to 700 nm to be collected, which precludes quantitative analysis of scattering near the plasmon resonance of the Ag nanoparticles at 414 nm. We therefore integrated the scattered intensity from 500 to 690 nm, corresponding to scattering from the slowly decaying (not very weak) tail on the long-wavelength side of the plasmon resonance. These integrated scattering intensities are shown in Figure 5b, and the corresponding optical images, obtained simultaneously (see Supporting Information, Movie S2), are shown in Figure 5a. The scattering increases approximately linearly with the number of particles, with only a small superlinear factor. This indicates that any interaction among the optically bound Ag nanoparticles is weak (see eqs 3, 4); this is in contrast to near-field interaction of plasmonic nanoparticles separated by tens of nanometers, which can cause enhanced resonant scattering.[19]

**Chains of Ag Nanoparticles in a Linear Light Field.** To study the long-distance optical binding of multiple Ag nanoparticles, we produced a highly anisotropic light field to confine the particles in a line. An image of this line trap can be seen in Figure 6a. Ag nanoparticles could move along the long axis of the light field, but were confined by a strong gradient force in the transverse direction. The half-waveplate was removed from the optical train to reduce possible phase-front distortion, and thus the polarization direction was fixed along the $x$-axis (at $\theta = 0°$). In order to change the relative orientation of the nanoparticle chains and the laser polarization, the line trap was rotated by "rotating" the phase mask on the SLM. We considered two cases, as illustrated in Figure 6a: in case I, the trap is parallel to the polarization direction ($\varphi = 0°$), and in case II, the trap is perpendicular to the polarization direction ($\varphi = 90°$). Figure 6b and c show representative images of chains of two to five Ag nanoparticles for the two trap orientations.

The nanoparticles in a chain exhibited correlated motion, tending to move together in the same direction at the same time. This can be seen in the particle trajectories at the bottom of Figure 6b and c and in the histograms of interparticle separations in Figure 6d. Adjacent particles have a preferred separation of approximately 600 nm, similar to the preferred interparticle separation in the cylindrically symmetric light field (see Figure 3). For next nearest neighbors and further neighbors, the separations are near integral multiples of 600 nm.

Moreover, we observe three trends for the chains of Ag nanoparticles that confirm the three theoretical predictions given above. (1) When $\varphi = 90°$, the equilibrium separation of adjacent particles is approximately 590 nm, slightly smaller than the approximately 600 nm separation when $\varphi = 0°$. In addition, the distribution of particle separations is narrower, indicating stronger binding. (2) When $\varphi = 90°$, the separation of adjacent particles shows a second maximum at about 1.1 $\mu$m. (3) When $\varphi = 90°$, nanoparticles in the chain are more likely to change positions with adjacent ones, and subgroups of dimers may form, as shown in the last image of Figure 6c (*i.e.*, subpanel #5).

We determined that the equilibrium separation is different for terminal pairs, or pairs of particles with one member at the end of the chain, as compared to pairs in the center of the chain. For example, in a chain of four particles, the 1−2 pair and the 3−4 pair are symmetric and are both terminal pairs, and the 2−3 pair is a central pair. We grouped the central pairs and terminal pairs separately and calculated the potentials of mean force (pmf) for each category from the corresponding distributions of pair separations:

$$\mathrm{pmf}(d_{ij}) = -k_B T \ln P(d_{ij}) \quad (6)$$

where $k_B$ is Boltzmann's constant, $T$ is absolute temperature, and $P(d_{ij})$ is the probability density of the interparticle separation $d_{ij}$. The results are plotted in Figure 7, with zero potential set at the minimum of

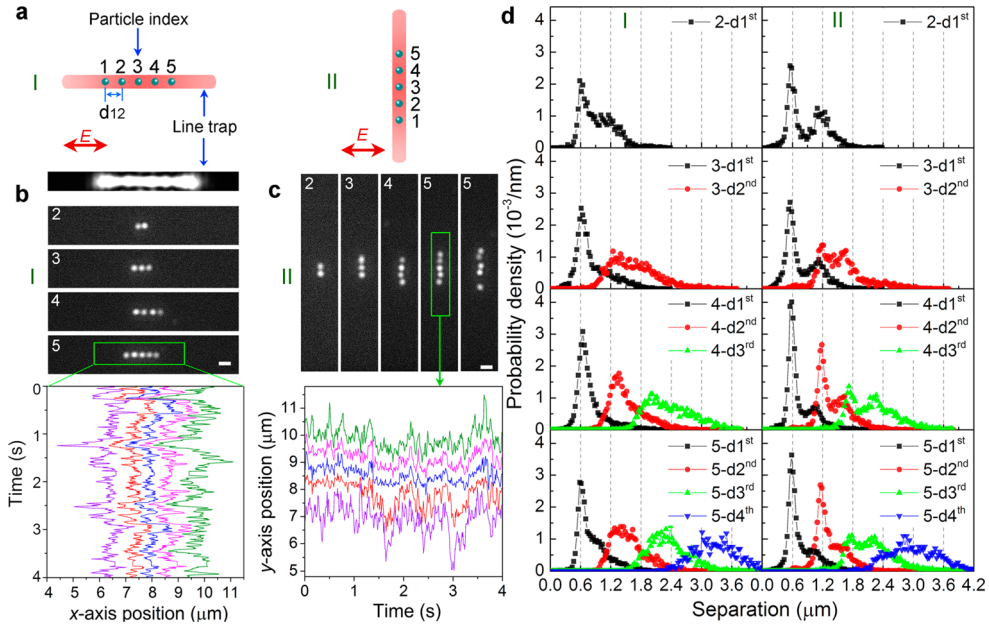


**Figure 6. Chains of Ag nanoparticles formed by optical binding in a line trap. (a) Schematics of the two configurations investigated: (I) the line trap is oriented parallel to the polarization direction (an optical image of the trap used in the experiment is also shown; some periodic nodes may be observed, which are imaging artifacts and are not present in the optical field the particles experience), and (II) the line trap is oriented perpendicular to the polarization direction. Sometimes, two particles may exchange positions; in this case, the particle indices are reassigned to make sure they are still in sequence. (b) Optical images of chains with two to five particles in the line trap corresponding to configuration I, and the trajectories of five particles in a chain. (See Supporting Information, Movie S3.) (c) Optical images of chains with two to five particles corresponding to configuration II and the trajectories of five particles in a chain. (See Supporting Information, Movie S4.) The white scale bars are 1 $\mu$m. (d) Histogrammed probability density functions of the separations between two particles in all the chains formed by optical binding. The distributions have been categorized by the relation of particle pairs in a chain: 1st, the nearest neighbors; 2nd, the next nearest neighbors; 3rd, the third nearest neighbors; and 4th, the fourth nearest neighbors. For example, 4-*d*2nd is a combination of $d_{13}$ and $d_{24}$ in a chain of four particles. The bin size is 30 nm.**

each curve. The results show that, under our experimental conditions, optical-binding potentials are several times larger than the thermal energy, $k_BT$. It is also clear that a second potential well exists for the terminal pairs when $\varphi = 90°$, but is not apparent for central pairs. Of course, since the chains tend to be close-packed, it is more difficult to sample larger separations for chains of more than two particles. This point will become important when comparing to the theoretical potentials described below.

Figure 7a clearly shows, for both $\varphi = 90°$ and $\varphi = 0°$, that the potential minima are sharper for the central pairs than for the terminal pairs, indicating that the central pairs are more stable. In other words, addition of nanoparticles to a chain increases the stability of the particles already in the chain. In case II ($\varphi = 90°$), the terminal pairs must overcome a free-energy barrier of about $2k_BT$ to move from the first equilibrium separation at approximately 600 nm to the second separation at approximately 1.1 $\mu$m and must overcome a barrier of about $1k_BT$ in the reverse direction. Thermal fluctuations can thus readily change the separation between these two positions. To verify that these features were determined by the orientation of the chain relative to the optical polarization rather than any possible beam distortions of the two traps, we did a control experiment by inserting the half-waveplate to the optical train to change $\theta$ to 90°; the second equilibrium separation then occurred for $\varphi = 0°$ instead of for $\varphi = 90°$ (see Supporting Information, Figure S5).

We also produced a longer line trap (see Figure 9a.I) and checked the optical binding of the 40 nm diameter Ag nanoparticles in this light field. Since the same amount of light (*i.e.*, constant power of incident beam) is spread over a larger area in this trap, the confining potential is weaker. Nonetheless, Ag nanoparticles still formed chains in this line trap, with equilibrium separation still around 600 nm, and other characteristics similar to those described above. In particular, the potential of mean force for the optical binding interaction was still several times $k_BT$, but the particles exhibited larger positional fluctuations (see Supporting Information, Figures S6 and S7).

It is worth noting that in the pmf plots (Figures 7a and S7) the optical binding potentials are apparent only over a small range of interparticle separations around the equilibrium separations. For larger separations, the interparticle interactions are affected by the potential of the line trap (see Supporting Information, Figure S8 and the note after Figure S6). As noted above for the centrosymmetric trap, the potential of the line trap pushes the particles closer together, so that the weak optical binding interaction is more apparent in the thermally sampled data. At the same time, the

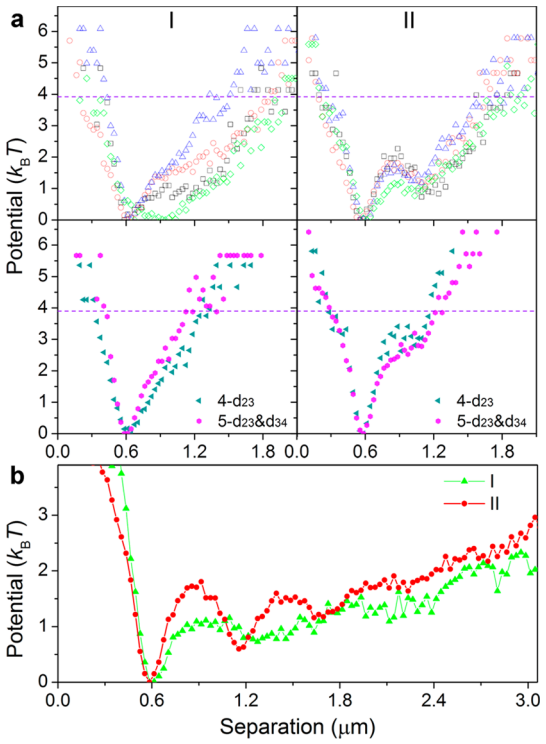


**Figure 7. (a) Potentials of mean force calculated from the distributions of interparticle separation for the chains corresponding to cases I and II shown in Figure 6d. The distributions have been categorized on the basis of the symmetry of the particle pairs in a chain. The top and bottom panels show the potentials for terminal and central pairs, respectively. The open symbols in the top panels represent 2-$d_{12}$ (the black squares), 3-$d_{12}$&$d_{23}$ (red circles), 4-$d_{12}$&$d_{34}$ (blue triangles), and 5-$d_{12}$&$d_{45}$ (green diamonds), respectively. Note that the points for vaules of the potentials greater than 3.9$k_BT$ (indicated by the horizontal dashed lines) represent separations with less than 2% of the maximum probability density for each curve and are thus of limited statistical significance. (b) Potentials of mean force calculated from the combination of separation distributions of all the possible particle pairs in the chains of five particles (*i.e.*, summing the counts used to calculate the distributions shown in the bottom panel of Figure 6d).**

confining potential reduces the probability of observing large interparticle separations. This means that few events are measured at large separations, and the corresponding statistical errors preclude accurate determination of the pmf at larger interparticle separations. On the other hand, longer chains would have smaller sampling bias that results from the typical end-on fluctuations of the chain (*i.e.*, chains grow or shrink from particles joining or leaving along the chain axis). Chains of *ca.* five particles are a reasonable compromise of these opposite tendencies. In Figure 7b, we combined the separation distribution of all the possible particle pairs in the chains of five particles and calculated the (less constrained) potentials of mean force. The curves clearly show an oscillatory potential of mean force for optical binding, which has larger (free) energy barriers in the perpendicular case (red dots).

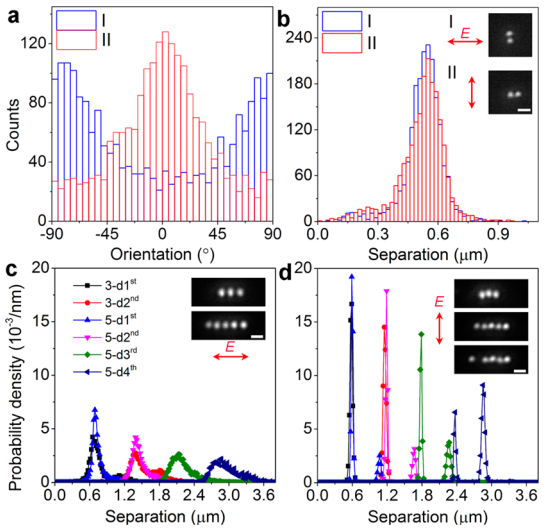


**Figure 8. Optical binding of 100 nm Ag nanoparticles (see Supporting Information, Figure S9). (a) Histograms of the dimer orientation and (b) histograms of the separation between particles in a dimer held in a cylindrically symmetric light field with polarization direction (I) $\theta = 0°$ and (II) $\theta = 90°$. The insets in (b) show the configurations and representative optical images. (c and d) Histogrammed probability density functions of the separations between two particles in chains with three and five particles in the longer line trap for the line trap oriented respectively parallel to and perpendicular to the optical polarization. The scale bars are 1 $\mu$m. Note that the optical binding interactions are strong enough that particle configurations can exist with gaps between the particles; that is, the particles can occupy the next-nearest minima in the binding potentials.**

**Optical Binding of Larger Ag Particles and the Formation of Synthetic Photonic Lattices.** In order to explore the interparticle interactions and structures that form when optical binding is stronger, we synthesized Ag nanoparticles with a mean diameter of approximately 100 nm. In the cylindrically symmetric light field, dimers of these 100 nm Ag nanoparticles tended to align perpendicular to the polarization direction (see Figure 8a) with a separation of about 550 nm (see Figure 8b). Figure 8c and d show probability density distributions of particle pairs in chains with three and five particles. The equilibrium separation is smaller when $\varphi = 90°$ than when $\varphi = 0°$, and the distribution of separations is much narrower. These observations are consistent with the previous theoretical calculations that predict stronger optical binding for polarization perpendicular to the axis of the chains. For $\varphi = 90°$, a second minimum also exists at approximately 1.1 $\mu$m for a terminal pair in the chain of five particles. Movie S7 in the Supporting Information shows the terminal nanoparticle jumping between the first equilibrium separation and the second one. Note that in the image shown in Figure 8d the three particles want to form a slightly triangular shape, but the tendency is restricted by the optical trapping potential.

The 100 nm Ag particles can also arrange into more complicated arrays, such as those shown in Figure 9a.

The structure of the lattices (clusters) can be adjusted by controlling the polarization direction. As shown in Figure 9a.II, when the polarization was parallel to the line direction ($\theta$ = 0°), a long chain of about 20 Ag nanoparticles could form. The equilibrium separation of adjacent particles is about 400 nm in this case, shorter than that in chains with only a few particles (see Figure 8c). This indicates the optical binding has been enhanced by collective interactions that extend across the long chain. When $\theta = -45°$, these nanoparticles formed dimers that were parallel to each other but were tilted relative to the major and minor axes of the trap (see Figure 9a.III). When $\theta = -90°$, a rectangular array could form, composed of optically bound nanoparticle dimers arranged in a line (see Figure 9a. IV). The lattice constant of the array is 580 nm in the *x*-direction and 340 nm in the *y*-direction. These optically bound lattices have a relatively low degree of symmetry, unlike the close-packed arrays that are typically formed through self-assembly of colloidal particles.[25,26] These results suggest than even more complex synthetic lattices of metal nanoparticles could be formed by optical binding through the application of properly designed structured light fields. In fact, Figure 9b shows a rigid cluster of 100 nm Ag nanoparticles that formed in the optical trap and that underwent rigid-body motion, with essentially no fluctuations in the interparticle separations. Such rigid clusters were not common in our experiments, although we observed many relatively stable chains (in which only the terminal particles had significant fluctuations). We believe that the specific geometry of this cluster may have contributed to its exceptional stability. However, this issue is beyond the scope of this paper since it requires appropriate numerical simulations to corroborate.

## DISCUSSION

**Comparison of Theory and Experiment.** The measurements of 40 nm Ag nanoparticles in the cylindrically symmetric light field confirm the theoretical predictions from the point dipole model that the particles will arrange into (nearly) compact assemblies separated by approximately 600 nm. For assemblies of three particles, the predicted distortions of the equilibrium configuration from an equilateral triangle are smaller than the error of the measurement, so we are unable to confirm this theoretical prediction. While all of the configurations shown in Figure 1 have zero in-plane forces and are stable with respect to small perturbations of any particle in any direction in the *xy*-plane, the three diamond-shaped rhombi appear closest to the geometries seen in experiment.

Ng *et al*. also predicted, through rigorous calculations, that optical binding could arrange Rayleigh particles into ordered geometric configurations, such as triangles, diamonds, and some metastable geometries, depending on the polarization direction.[22] So far there are no clear demonstrations of these predictions, although similar ordered lattices of sub-micrometer particles formed by optical binding in evanescent light fields have been observed.[27,28] Our experimental results agree well with these predictions.

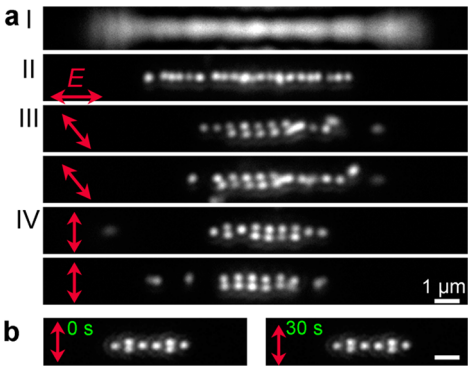


**Figure 9. Lattice-like particle configurations of 100 nm diameter Ag nanoparticles in a line trap. (a) Panel I is an image of a line trap resulting from trapping laser light scattering from the coverslip (again the image is distorted due to interference effects, but the actual field is smooth and continuous). Panels II–IV show representative images of Ag nanoparticle assemblies formed by optical binding in the line trap, for different polarization directions. (See Supporting Information, Movie S8.) (b) Results from another experiment with the 100 nm Ag nanoparticles. This cluster of eight particles is rigid and undergoes Brownian motion as a unit (see Supporting Information, Movie S9).**

For chains of 40 nm Ag nanoparticles in a linear optical field, we have shown that the observations agree well with the three theoretical predictions that we made: (1) polarization perpendicular to the chain gives stronger optical binding than polarization parallel to the chain; (2) for perpendicular polarization, a second equilibrium separation exists at (slightly less than) twice the first equilibrium separation (*e.g.*, see Figure 7b); and (3) addition of particles to a chain increases the strength of optical binding for particles already in the chain. The second observation, in particular, suggests an oscillatory potential surface for optical binding. To investigate this using the coupled dipole model, we started from the regular configurations shown in Figures S1 and S2 and moved a terminal particle along the axis of the chain keeping all other particles fixed in place. Integrating the force the particle experiences generates a potential energy function. As seen in Figure 10, parallel polarization ($\varphi$ = 0°) results in a weak potential that is attractive at small distances. By contrast, perpendicular polarization ($\varphi$ = 90°) results in a potential that is repulsive at short distances and that exhibits a regular series of potential wells at longer distances, the deepest two of which correspond to the distances observed in the experimental data.

It is worth noting that although the curves in Figure 7b are similar to those in Figure 10b, there are

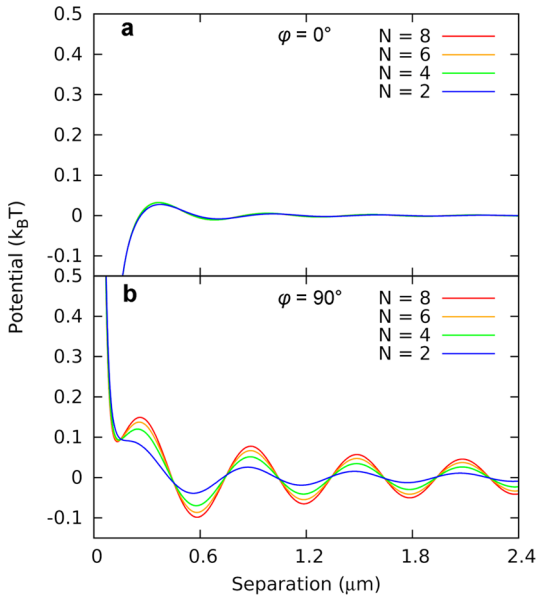


**Figure 10. Calculated potential energy curves in units of $k_BT$, where $T$ = 298 K, for optical binding of 40 nm Ag nanoparticles. Each curve is calculated by taking the integral of the optical binding forces given by eq 5 when a terminal particle in an $N$-particle chain is moved from its equilibrium position, with the remaining $N - 1$ particles remaining fixed. The zero of potential is taken to correspond to infinite particle separation. The incident light propagates in the $z$-direction and is polarized in the $x$-direction. The force and potential are evaluated along the direction of the chain oriented along the $x$-direction in (a) and along the $y$-direction in (b). The parameters for the calculation are chosen to match the experimental conditions.**

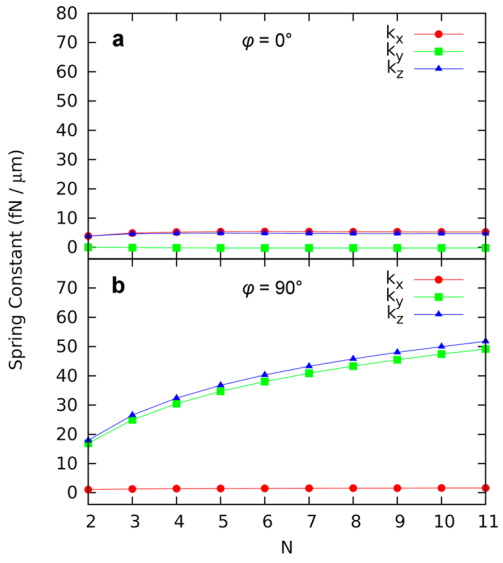


**Figure 11. Calculated spring constants for a terminal particle near equilibrium in chains of optically bound nanoparticles, as a function of chain length, for light fields polarized (a) parallel and (b) perpendicular to the chain. The incident light propagates in the $z$-direction and is polarized in the $x$-direction. The chain is oriented along the $x$-direction in (a) and along the $y$-direction in (b).**

differences. First, the curves in Figure 10b are calculated from optical forces where only a terminal particle is movable and the rest are fixed. The curves in Figure 7b are calculated from a sum of conditional probability densities where all the particles are movable, and the total potential experienced by a particle will be the result of both the optical-binding potential and the confining potential of the optical trap. Second, the attractive force in Figure 10a diverges more rapidly for small distances than the repulsive force in Figure 10b. In principle, the attractive force at small distances for $\varphi = 0°$ should bring the particles together to form closely packed aggregates. On the other hand, in the experiments, this phenomenon was not observed; that is, we never observed particle "fusion" for 40 nm particles. Several reasons may lead to the difference: (1) the Ag nanoparticles are coated with a polyvinylpyrrolidone (PVP) layer. The steric effect of the PVP layer prevents the nanoparticle surfaces from coming into close contact. (2) The Ag nanoparticles are also charged (the zeta potential of the as-received sample is −35.6 mV, and the magnitude is larger than the thermal voltage of $k_BT/e = 25$ mV at room temperature), leading to a long-range electrostatic repulsion that could prevent the particles from approaching closely. (3) We expect there to be a thermophoretic force due to laser-heating of the nanoparticles that tends to keep them apart. (4) At short distances (*ca.* particle diameter) there is a hydrodynamic lubrication force that retards the particles as they approach each other. (5) The calculation considers the particles as point dipoles, but this point dipole approximation breaks down as the separation decreases to a distance comparable to the particle diameter, which might affect the attractive interaction at small separations. More rigorous calculations are required to understand this regime.

Figure 11 shows calculated spring constants for optical binding of the terminal particles in chains of varying length. It is immediately clear that $\varphi = 90°$ gives dramatically larger spring constants than $\varphi = 0°$. This difference is the basis of our explanation for the anomalous polarization dependence for the dimers in the centrosymmetric trap. For $\varphi = 0°$, the spring constant in the $y$-direction is actually negative for chains of three or more particles, resulting in a destabilizing force that counteracts the constraining gradient force from the line trap itself. For $\varphi = 90°$, the spring constant is positive, resulting in stable binding of the particle in all three directions and reinforcing the gradient force that arises from the shaped optical fields. The most important spring constant is that in the direction of the chain axis, since the trapping field itself does not explicitly constrain the particles in this direction, except for a gradient at the ends of the line trap. The spring constant calculation in Figure 11 was repeated for particles in the interior of chains. We found that the trends are identical, while the

magnitude of the forces is several times larger, which explains our experimental observation that central pairs in the chains are more stable than terminal pairs. Finally, we note that the stabilizing spring constants in the $\varphi = 90°$ case grow more slowly than linearly with chain length even before accounting for thermal disorder in the arrangements. This subextensive scaling may compromise the ability of optical binding to form chains of unlimited length.

**Factors Affecting the Calculations.** The trends predicted by all of the aforementioned calculations for the 40 nm nanoparticles are consistent with the experimental results, but the predicted spring constants and depths of the potential wells in Figure 10 are smaller than the values determined experimentally (shown as the pmf's). We first note that potential energy functions are not the same as potentials of mean force, but they can be compared when entropic factors are not dominant. A more accurate comparison would be obtained by running Langevin dynamics or Monte Carlo simulations using forces as calculated here. This is beyond the scope of the present paper.

There are other factors that should be made clear. Taken at face value in the limit of two particles, the experimental and theoretical results in Figures 7a.II and 10b differ by a factor of approximately 17 (or a factor of ~10 for the results shown in Figure 7b). The shallow Gaussian intensity profile along the line trap, which imparts a compressive gradient force on the particles, will contribute to the discrepancy since the calculations assume uniform plane wave illumination and no gradient in the incident optical field. This confinement from the trap accounts for the growth of the pmf at large separations (see Figure 7) and also creates ambiguities in the intensity that is assumed for the plane wave illumination in the calculations.

The calculations have a strong, approximately quadratic dependence of the binding forces on the particle polarizabilities.[16] The accuracy of the polarizability, in turn, is affected by (i) the significant uncertainties in the tabulated values of the dielectric function that are used for the calculations; (ii) even slight deviations of the particle shape from perfect sphericity; and (iii) variations in the particle size, varying approximately as the third power of the particle diameter. It is reasonable to expect that the largest, most polarizable particles in an ensemble would be seen disproportionately often in an optical trap, and this could significantly increase the measured optical-binding forces. To illustrate this point, we recalculated the potentials from Figure 10 but for spherical particles with a diameter of 50 nm, corresponding to the largest particles seen in the colloidal sample with a mean diameter of 40 nm. Results are shown in Figure S10 of the Supporting Information and demonstrate that the relatively modest 25% increase in the particle diameter increases the optical-binding forces and energies by a factor of 4.5. However, the trends and shapes of the potentials remain nearly identical, as do the equilibrium geometries. Even for 100 nm nanoparticle diameters, the calculations predict nearly identical geometries and trends for the forces. These theoretical predictions can thus be considered robust, even if the magnitudes of the forces are less well specified.

One behavior that is not seen in our calculations is the formation of unusual 2D synthetic lattices from optical binding of 100 nm Ag particles (Figure 9). We believe that these larger particles can no longer be accurately approximated as point dipoles, so that our model cannot predict this more complex behavior. The large size results in retardation effects, so higher order terms in a multipole expansion of the fields in eqs 2 and 3 would be required. We show the potentials of mean force curves calculated from the data of chains of five 100 nm Ag particles in Figure S11 of the Supporting Information. These pmf's are different from the shape of curves shown in Figure 10 (and S10). We believe that the experimental pmf's reflect strong binding effects that are expected to arise due to the multipole interactions. Therefore, more complicated numerical calculations would be needed to explain the interactions of these larger particles with light fields.

## CONCLUSIONS

We have shown that optical binding can induce self-assembly of Ag nanoparticles in aqueous solution. Our measurements demonstrate the extension of optical binding into the Rayleigh regime.[22] We have also shown that the optical binding of larger Ag nanoparticles enables the controlled formation of two-dimensional nanoparticle arrays or synthetic photonic lattices. Together, these results enable a number of exciting opportunities. Demergis and Florin have shown that the optical binding forces could be applied to trap a smaller gold particle between a pair of larger gold particles, due to the large field gradients between the two larger particles.[20] We believe that optically bound lattices of metal nanoparticles will allow similar co-trapping of smaller and less polarizable nanoparticles such as semiconductor quantum dots or perhaps even biological macromolecules. This possibility will be enhanced by increasing the polarizability of the optically bound nanoparticles, which can be accomplished by using nonspherical metal nanoparticles or by tuning the trapping laser wavelength so that the optical field is close to plasmon resonances in the particles.[29,30] In this way, new hybrid assemblies with strong nonlinear-optical and quantum-optical properties may be "synthesized" by purely optical means. Assembly of different-sized metal nanoparticles into controlled arrays may also enable the construction of sensors,

phased-element optical arrays, superradiant devices,[31] and tunable "superlenses".[32] Finally, the assembly of these arrays in solution could be followed by pushing the assembly to a properly functionalized surface to create permanent nanoparticle configurations for various applications.[30,33]

## METHODS

**Ag Nanoparticles.** The 40 nm Ag nanoparticles were purchased from nanoComposix, Inc. (NanoXact Ag nanoparticles). The reported diameters are 40.3 nm with a standard deviation of 3.5 nm. The particles are coated with PVP to prevent aggregation and are dispersed in water. We diluted the colloidal solution with water and added glycerol into the solution (10% v/v) to increase the viscosity and thus to slow down the Brownian motion of these small particles.

The 100 nm Ag nanoparticles were synthesized *via* polyol reduction of $AgNO_3$. In a typical synthesis, 5 mL of ethylene glycol (EG) was added to a glass vial with a stir bar and heated to 120 °C in an oil bath. A 0.75 mL sample of 0.147 M (by monomer) PVP (average molecular weight of 55 000) in EG was then injected into the heated EG, followed by 0.75 mL of 0.094 M $AgNO_3$ in EG. The vial was sealed with a cap, kept at 120 °C for 80 min, and then rapidly cooled to room temperature in a water bath. The products were centrifuged and washed with acetone once and with water several times. The particles were finally dispersed in water and centrifuged at 2000 rpm for 10 min. The remaining suspension was further diluted by water and used for the optical binding experiments. Figure S9 in the Supporting Information shows an SEM image of the Ag nanoparticles from the final sample and the size distribution of the particles.

**Optical System.** Details of the optical-tweezers apparatus have been described previously.[34,35] The structured light fields were generated by a spatial light modulator (SLM, Hamamatsu Photonics X10468 Series). To produce the Bessel beam, an axicon phase mask was applied to the SLM, and three lenses were placed between the SLM and the objective.[34] To produce the line traps, cylindrical-lens phase masks were applied to the SLM, and two lenses were placed between the SLM and the objective (producing a 4*f* system).[35] We note that, due to the limited filling factor of the SLM, approximately 5% of the incident light is not diffracted by the SLM and, thus, adds an extra feature to the structured light; however, the trapping potential due to this undiffracted light is much weaker than the optical binding potentials and does not influence the experiments with more than two particles. For the longer line trap, we added a blazed-grating phase mask to the cylindrical-lens phase mask on the SLM, thereby shifting the line trap away from the undiffracted beam.[36]

The laser power after the objective was measured to be approximately 100 mW. The Ag nanoparticles were visualized by dark-field microscopy, using a high numerical-aperture dark-field condenser (Olympus, U-DCW, NA = 1.4) and a 60× water-immersion objective (NA 1.2, Olympus UPLSAPO, NA = 1.2). Two beam expanders (1.6× and 2×) were used to further magnify the optical images incident on the cameras used to record videos of the trapped particles. The videos of Ag nanoparticles in the Bessel beam trap were recorded using an sCMOS camera (Andor Neo), and those in the line traps were recorded using a Firewire CCD camera (Sony XCD-V60). Trajectories of the nanoparticles were extracted from the optical images using commercial software (DiaTrack). The dark-field scattering spectra were collected using a spectrometer (Ocean Optics, USB 2000) coupled to a 400 $\mu$m fiber, which collected light from a 4 $\mu$m diameter spot in the sample cell. The spectra were normalized to the spectrum of light scattered from a bare coverslip surface. The correlated optical images were recorded using the Sony camera.

**Analytical Calculations.** Optical-binding forces are determined on the basis of eq 5. In the current study, we consider the case of *N* identical spheres, so that $\alpha_{st}^{(n)} = \alpha\delta_{st}$ for all *n*. We computed the effective polarizability, $\alpha$, by first finding the extinction and scattering cross sections of a silver sphere using Mie theory.[37] We then used these cross sections to solve for the real and imaginary parts of the polarizability within the electrostatic model for a vanishingly small sphere.[37] Except where noted, the particle radius was taken to be 20.15 nm. The complex dielectric constant of Ag at 1.55 eV was obtained by fitting the data in ref 38 to a spline. The dielectric constant of the medium is based on the $n = 1.347$ refractive index of a 10% by volume (12% by mass) solution of glycerol in water.[39] Together, these assumptions give rise to a polarizability $\alpha = (2.057 \times 10^{-33} + 2.230 \times 10^{-35}\mathrm{i})$ $Cm^2/V$, in the notation of ref 16; this is within 5% of the prediction of the dipole theory with a radiative reaction correction.[16]

The incident field is taken to be a plane wave propagating in the *z*-direction and polarized in the *x*-direction. We take the perspective in the calculations that the shaped optical fields merely present constraints for the particles' positions: particles are located near the region of maximum intensity, where the gradient of the field is zero, except for a slight displacement in the *z*-direction due to radiation pressure from the incident laser.

The incident electric field strength corresponds to the intensity at the center of the shorter line trap used in Figure 6. This intensity was found by performing a two-dimensional Fourier transform of the SLM phase mask, accounting for a 12 mm diameter aperture at the SLM, setting the length scale by matching the calculated trap length at 10% of peak intensity to the 8.4 $\mu$m measured length of the trap, and matching the integrated intensity of the calculated trap to the 100 mW measured laser power exiting the objective. This procedure gave an intensity of 14 $MW/cm^2$ at the center of the line trap. Geometry optimizations of optically bound nanoparticles were performed by finding configurations for which the in-plane forces $F_x^{(n)}$ and $F_y^{(n)}$ are all equal to zero, using a simplex minimization search algorithm.

In order to obtain the zero-force configurations of the chains, we seeded the search algorithm with 675 nm interparticle spacing and 575 nm spacing for parallel and perpendicular polarizations, respectively. Isosceles triangles, rhombi, and rectangles were constrained to those shapes by using their respective symmetries in parametrizing the minimization. Spring constants were found by displacing a particle of interest by 1 nm in an appropriate direction, holding all other particles at their equilibrium configurations, and calculating the restoring force on the displaced particle; for spring constants in the *z*-direction, the force on the particle is nonzero due to radiation pressure, so we use a difference of forces to compute an effective spring constant. Optical binding potentials were found by integrating the forces over a 1 nm mesh parallel to the chain direction.

*Conflict of Interest:* The authors declare no competing financial interest.

*Acknowledgment.* This work was supported by the National Science Foundation (CHE-1059057). We acknowledge the University of Chicago NSF-MRSEC (DMR-0820054) for central facilities. R.A.S. was supported by a National Science Foundation Graduate Research Fellowship. This work was performed, in part, at the Center for Nanoscale Materials, a U.S. Department of Energy, Office of Science, Office of Basic Energy Sciences User Facility, under Contract No. DE-AC02-06CH11357.

*Supporting Information Available:* Video clips showing the optical binding of Ag nanoparticles and additional figures. This material is available free of charge *via* the Internet at http://pubs.acs.org.

## REFERENCES AND NOTES

1. Xia, Y. N.; Gates, B.; Li, Z. Y. Self-Assembly Approaches to Three-Dimensional Photonic Crystals. *Adv. Mater.* **2001**, *13*, 409–413.

2. Whitesides, G. M.; Grzybowski, B. Self-Assembly at All Scales. *Science* **2002**, *295*, 2418–2421.
3. Lin, Y.; Boker, A.; He, J. B.; Sill, K.; Xiang, H. Q.; Abetz, C.; Li, X. F.; Wang, J.; Emrick, T.; Long, S.; *et al*. Self-Directed Self-Assembly of Nanoparticle/Copolymer Mixtures. *Nature* **2005**, *434*, 55–59.
4. Grzelczak, M.; Vermant, J.; Furst, E. M.; Liz-Marzan, L. M. Directed Self-Assembly of Nanoparticles. *ACS Nano* **2010**, *4*, 3591–3605.
5. Zeng, J.; Zheng, Y.; Rycenga, M.; Tao, J.; Li, Z.-Y.; Zhang, Q.; Zhu, Y.; Xia, Y. Controlling the Shapes of Silver Nanocrystals with Different Capping Agents. *J. Am. Chem. Soc.* **2010**, *132*, 8552–8553.
6. Egusa, S.; Redmond, P. L.; Scherer, N. F. Thermally-Driven Nanoparticle Array Growth from Atomic Au Precursor Solutions. *J. Phys. Chem. C* **2007**, *111*, 17993–17996.
7. Mann, S. Self-Assembly and Transformation of Hybrid Nano-Objects and Nanostructures under Equilibrium and Non-Equilibrium Conditions. *Nat. Mater.* **2009**, *8*, 781–792.
8. Winkleman, A.; Gates, B. D.; McCarty, L. S.; Whitesides, G. M. Directed Self-Assembly of Spherical Particles on Patterned Electrodes by an Applied Electric Field. *Adv. Mater.* **2005**, *17*, 1507–1511.
9. Burns, M. M.; Fournier, J. M.; Golovchenko, J. A. Optical Binding. *Phys. Rev. Lett.* **1989**, *63*, 1233–1236.
10. Burns, M. M.; Fournier, J. M.; Golovchenko, J. A. Optical Matter: Crystallization and Binding in Intense Optical Fields. *Science* **1990**, *249*, 749–754.
11. Svedberg, F.; Li, Z.; Xu, H.; Käll, M. Creating Hot Nanoparticle Pairs for Surface-Enhanced Raman Spectroscopy through Optical Manipulation. *Nano Lett.* **2006**, *6*, 2639–2641.
12. Tong, L.; Righini, M.; Gonzalez, M. U.; Quidant, R.; Käll, M. Optical Aggregation of Metal Nanoparticles in a Microfluidic Channel for Surface-Enhanced Raman Scattering Analysis. *Lab Chip* **2009**, *9*, 193–195.
13. Banik, M.; El-Khoury, P. Z.; Nag, A.; Rodriguez-Perez, A.; Guarrottxena, N.; Bazan, G. C.; Apkarian, V. A. Surface-Enhanced Raman Trajectories on a Nano-Dumbbell: Transition from Field to Charge Transfer Plasmons as the Spheres Fuse. *ACS Nano* **2012**, *6*, 10343–10354.
14. Tatarkova, S. A.; Carruthers, A. E.; Dholakia, K. One-Dimensional Optically Bound Arrays of Microscopic Particles. *Phys. Rev. Lett.* **2002**, *89*, 283901.
15. Čižmár, T.; Romero, L. C. D.; Dholakia, K.; Andrews, D. L. Multiple Optical Trapping and Binding: New Routes to Self-Assembly. *J. Phys. B: At. Mol. Opt. Phys.* **2010**, *43*, 102001.
16. Dholakia, K.; Zemánek, P. Colloquium: Gripped by Light: Optical Binding. *Rev. Mod. Phys.* **2010**, *82*, 1767–1791.
17. Summers, M. D.; Dear, R. D.; Taylor, J. M.; Ritchie, G. A. D. Directed Assembly of Optically Bound Matter. *Opt. Express* **2012**, *20*, 1001–1012.
18. Rodriguez, J.; Davila Romero, L. C.; Andrews, D. L. Optical Binding in Nanoparticle Assembly: Potential Energy Landscapes. *Phys. Rev. A* **2008**, *78*, 043805.
19. Zelenina, A. S.; Quidant, R.; Nieto-Vesperinas, M. Enhanced Optical Forces between Coupled Resonant Metal Nanoparticles. *Opt. Lett.* **2007**, *32*, 1156–1158.
20. Demergis, V.; Florin, E.-L. Ultrastrong Optical Binding of Metallic Nanoparticles. *Nano Lett.* **2012**, *12*, 5756–5760.
21. Novotny, L.; Hecht, B. *Principles of Nano-Optics*.: Cambridge University Press, 2006.
22. Ng, J.; Lin, Z. F.; Chan, C. T.; Sheng, P. Photonic Clusters Formed by Dielectric Microspheres: Numerical Simulations. *Phys. Rev. B* **2005**, *72*, 085130.
23. Chaumet, P. C.; Nieto-Vesperinas, M. Time-Averaged Total Force on a Dipolar Sphere in an Electromagnetic Field. *Opt. Lett.* **2000**, *25*, 1065–1067.
24. Qu, X. H.; Wu, D.; Mets, L.; Scherer, N. F. Nanometer-Localized Multiple Single-Molecule Fluorescence Microscopy. *Proc. Natl. Acad. Sci. U.S.A.* **2004**, *101*, 11298–11303.
25. Norris, D. J.; Arlinghaus, E. G.; Meng, L. L.; Heiny, R.; Scriven, L. E. Opaline Photonic Crystals: How does Self-Assembly Work? *Adv. Mater.* **2004**, *16*, 1393–1399.
26. Zhang, J.; Li, Y.; Zhang, X.; Yang, B. Colloidal Self-Assembly Meets Nanofabrication: From Two-Dimensional Colloidal Crystals to Nanostructure Arrays. *Adv. Mater.* **2010**, *22*, 4249–4269.
27. Mellor, C. D.; Bain, C. D. Array Formation in Evanescent Waves. *ChemPhysChem* **2006**, *7*, 329–332.
28. Mellor, C. D.; Fennerty, T. A.; Bain, C. D. Polarization Effects in Optically Bound Particle Arrays. *Opt. Express* **2006**, *14*, 10079–10088.
29. Pelton, M.; Liu, M.; Kim, H. Y.; Smith, G.; Guyot-Sionnest, P.; Scherer, N. F. Optical Trapping and Alignment of Single Gold Nanorods by Using Plasmon Resonances. *Opt. Lett.* **2006**, *31*, 2075–2077.
30. Guffey, M. J.; Miller, R. L.; Gray, S. K.; Scherer, N. F. Plasmon-Driven Selective Deposition of Au Bipyramidal Nanoparticles. *Nano Lett.* **2011**, *11*, 4058–4066.
31. Le, F.; Brandl, D. W.; Urzhumov, Y. A.; Wang, H.; Kundu, J.; Halas, N. J.; Aizpurua, J.; Nordlander, P. Metallic Nanoparticle Arrays: A Common Substrate for Both Surface-Enhanced Raman Scattering and Surface-Enhanced Infrared Absorption. *ACS Nano* **2008**, *2*, 707–718.
32. Li, K.; Stockman, M. I.; Bergman, D. J. Self-Similar Chain of Metal Nanospheres as an Efficient Nanolens. *Phys. Rev. Lett.* **2003**, *91*, 227402.
33. Guffey, M. J.; Scherer, N. F. All-Optical Patterning of Au Nanoparticles on Surfaces Using Optical Traps. *Nano Lett.* **2010**, *10*, 4302–4308.
34. Yan, Z.; Sweet, J.; Jureller, J. E.; Guffey, M. J.; Pelton, M.; Scherer, N. F. Controlling the Position and Orientation of Single Silver Nanowires on a Surface Using Structured Optical Fields. *ACS Nano* **2012**, *6*, 8144–8155.
35. Yan, Z.; Jureller, J. E.; Sweet, J.; Guffey, M. J.; Pelton, M.; Scherer, N. F. Three-Dimensional Optical Trapping and Manipulation of Single Silver Nanowires. *Nano Lett.* **2012**, *12*, 5155–5161.
36. Bowman, R.; D'Ambrosio, V.; Rubino, E.; Jedrkiewicz, O.; Di Trapani, P.; Padgett, M. J. Optimisation of a Low Cost SLM for Diffraction Efficiency and Ghost Order Suppression. *Eur. Phys. J. Spec. Top.* **2011**, *199*, 149–158.
37. Bohren, C. F.; Huffman, D. R. *Absorption and Scattering of Light by Small Particles*; Wiley-VCH Verlag GmbH: Weinheim, 2007.
38. Johnson, P. B.; Christy, R. W. Optical Constants of the Noble Metals. *Phys. Rev. B* **1972**, *6*, 4370–4379.
39. Basker, D. Relationship between Refractive Index and Specific Gravity of Aqueous Glycerol Solutions. *Analyst* **1978**, *103*, 185–186.